ARTICLE TYPE

Sol-Gel Synthesis of Zinc Ferrite-Based Xerogel Monoliths with Well-Defined Macropores

Yasuki Kido, Kazuki Nakanishi,* and Kazuyoshi Kanamori

Starting from an aqueous solution, porous zinc ferrite-based xerogel monoliths have been prepared via sol-gel route accompanied by phase separation mediated by propylene oxide in the presence of poly(acrylamide). The xerogels possess well-defined macropores, and the macroporous morphologies could be easily controllable (macropore size ranges from 0.55 to 1.29 µm) by simply changing the

10 starting composition. As-dried xerogel samples were amorphous under X-ray diffraction, while heat-treatment in air brought about the formation of spinel type ferrite phase, $ZnFe_2O_4$. Calcination under Ar atmosphere allowed the crystallization of various iron-based phases/carbon composites (Fe_3O_4, $Fe_{1-\delta}O$, Fe_3N, Fe_4N, Fe_3C, and Fe). Samples heated under Ar flow exhibited hierarchical pore structures, including continuous macropores, in addition to mesopores and micropores embedded in the carbon-

15 containing composite matrices.

Introduction

Metal oxides composed of multiple metal ions with different valences often crystallize in characteristic structures such as spinel and perovskite; spinel type mixed oxides are major
20 materials for pigments, catalysts, and magnetic media and so on.[1] Among them, ferrite, iron oxide-based mixed metal oxide, has been extensively studied due to its unique property. Spinel type ferrite (MFe_2O_4; M = Mn, Zn, Co, Cu, Ni etc.) is a well-known magnetic material, called "soft-ferrite", and finds a variety of
25 applications in industry. Owing to its remarkable properties controlled by the relative concentration of constituent cations,[2] such as high magnetic permeability, high electric resistance and low eddy-current loss, the soft-ferrites have been used in various fields: inductance materials for high-frequency, magnetic cores,
30 shielding materials, and magnetic separation filter as well as catalyst, adsorbent, and electrode.[3] Hexagonal type ferrite ($MFe_{12}O_{19}$; M = Ba, Sr etc.) and garnet type ferrite (MFe_5O_{12}; M = Y etc.) have been applied for, for example, microwave absorber and so on.[4] Recently, porous ferrite including several
35 morphologies has been actively synthesized.[5] For these applications, in the case of conventional particulate materials, it is essential to control the morphology in a length scale from nanometer to micrometer, in addition to the surface area and particle size distributions.[6] On the other hand, monolithic porous
40 materials with high surface area have been utilized as separation media and catalysts owing to their characteristic "co-continuous" macroporous structure that facilitates fast transport of external liquid or gas into the pore surfaces.[7] The properties of ferrite that depend on the accessibility of external molecules to their internal
45 surfaces, such as catalytic and adsorption efficiency, will be enhanced by shaping it into a monolithic form with an optimized pore structure. In the present study, as the first demonstration of preparation of monolithic porous ferrite, we report synthesis of macroporous ferrite-based monolith, zinc ferrite ($ZnFe_2O_4$).

50 Different routes for producing ferrite in a monolithic form have been reported; roughly categorized into solid state or wet chemical methods. Wet chemical synthesis of zinc ferrite includes co-precipitation, hydrothermal method, sonochemical route, reverse micelle method, thermolysis technique, and sol-gel
55 reaction.[8] Among others, sol-gel approach has a potential of broad practical applications because it offers facile and homogeneous route to varied morphologies. Sol-gel-derived materials are often prepared using metal alkoxides, for example, tetramethylorthosilicate (TMOS), as precursors. The extension to
60 mixed metal oxide system by the sol-gel method, however, is not straightforward. Not a few disadvantages such as high reactivity, inhomogeneity in alkoxide mixture, and the unavailability of alkoxides containing specific metals, prevent one from obtaining desired crystalline phases and to control morphologies. In order
65 to prepare homogeneous mixed metal oxides, it is necessary to choose appropriate precursors; bimetallic alkoxide, or non-alkoxides system.[9] Non-alkoxide sol-gel route using cyclic ether was first reported by Gash *et al.* in 2001.[10] Starting from metal salts, a cyclic ether such as propylene oxide is protonated from
70 metal hydrate species, followed by the ring opening to form substituted alcohols, playing a role of "acid scavenger". The irreversible and *in situ* consumption of acid from the starting composition is advantageous to induce homogeneous hydrolysis and condensation of aquo-cations. The route ensures a process at
75 low temperature, with low cost and minimal reaction steps. Furthermore, the cyclic ether route can be applied to systems containing various metals; main group, transition, and rare earth.[11,12] It is in general easy to be extended to mixed metal oxide system.[13,14] Materials having different morphological
80 features such as aerogels, thin film, and particles thus have been prepared by the above synthetic method.
Utilizing the epoxide-mediated sol-gel system, monolithic macroporous alumina has been recently prepared.[15] Combining the above reaction with polymerization-induced phase separation,

the spatial freezing of the transitional "co-continuous" structure led to the formation of well-defined macropores after drying.[16] The method has been used for the synthesis of monolithic macroporous mixed metal oxide, containing tri-, di-, or mono-valent cations.[17] Recently, we have already reported the synthesis of iron(III)-based xerogel monolith via sol-gel route with phase separation.[18] In the previous paper, it has been revealed that the use of polyols as an additive solvent effectively inhibited uncontrolled precipitation of iron(III) (oxy)hydroxide to produce co-continuous macroporous structures in a monolithic from. As an extension of the preceding research, macroporous zinc ferrite-based monoliths were synthesized in the present study from ionic precursors, iron(III) chloride hexahydrate and zinc(II) chloride, in water-glycerol solvents. Macroporous morphology, macropore size and pore volume, could be easily controllable by changing the starting composition. The effect of calcination condition (air or Ar) on macrostructure and crystalline phase was examined and compared with that in pure iron(III) oxide system.

Experimental Section

Synthesis

In a glass tube, 1.61 g of $FeCl_3 \cdot 6H_2O$ (Sigma-Aldrich, USA, 99+%), 0.41 g of $ZnCl_2$ (Sigma-Aldrich, USA, 99+%) (Zn/Fe, R = 0.50 in molar ratio), and W_{PAAm} g of PAAm (Poly(acrylamide); Sigma-Aldrich, USA, 50 wt% in water, with average molecular weight of 10,000) were dissolved in a mixture of 2.00 mL of distilled water and 2.00 mL of glycerol (Kishida Chemical, Japan, 99.8%) to give a clear orange solution. Alternatively, some samples with varied amount of solvents V_{H2O} of distilled water and/or V_{GLY} of glycerol, setting the total volume of V_{H2O} and V_{GLY} at 4.00 mL, were synthesized. The addition of 1.88 mL of PO (Propylene Oxide; Sigma-Aldrich, USA, 99%) to the mixed solution ([PO]/{[Zn]+[Fe]} = 3 in molar ratio) at 30 ℃ formed light brown opaque gel within 2-3 min. Some samples were prepared with varied R (from 0.20 to 2.00) or without adding iron(III) chloride hexahydrate (only zinc chloride as a metal source), setting the total metal molar quantity identical to the other samples. The glass tube containing precursor solution was sealed and kept at 60 ℃ for gelation, aged at 80 ℃ for 24 h, immersed in 2-propanol (Kishida Chemical, Japan, >99%) for 24 h at 60 ℃ three times, and then evaporation dried at 40 ℃. Heat-treatment in air for 4 h was carried out for some samples at temperatures up to 400 ℃ with a heating rate of 5 ℃ min^{-1}, whereas calcination under Ar flow (1 L min^{-1}) for 4 h was conducted at different temperatures up to 1000 ℃ at a heating rate of 5 ℃ min^{-1}.

Characterization

Microstructures of samples were observed by a scanning electron microscope (SEM: JSM-6060, JEOL, Ltd., Japan, with Pt coating). Elemental analysis was carried out by energy-dispersive X-ray spectrometer (EDX: JED-2300, JEOL, Ltd., Japan). Thermogravimetry (TG) and differential thermal analysis (DTA) (Thermo plus TG 8120, Rigaku Corp., Japan) measurement were performed on samples at a heating rate of 5 ℃ min^{-1} supplying air at a rate of 100 mL min^{-1} from room temperature to 1000 ℃. Chemical bonding analysis was measured by Fourier transform infrared spectroscopy (FT-IR: IR Affinity-1, Shimadzu Corp., Japan) using the KBr method; each spectrum was collected after 100 scans for the wavenumber range 400-4,000 cm^{-1} at a resolution of 2 cm^{-1}. Mercury porosimetry (Poremaster 60-GT, Quantachrome Instruments, USA) was used to characterize the macropore of samples from 10 nm to 300 µm. Micro/mesoporous structure was investigated by nitrogen adsorption-desorption apparatus (Belsorp mini II, Bel Japan Inc., Japan). The pore size distribution was estimated by Barrett-Joyner-Halenda (BJH) method using the adsorption branch, and specific surface area was calculated by Brunauer-Emmett-Teller (BET) method. The X-ray diffraction (XRD) patterns with CuKα radiation (λ = 0.154 nm) (RINT-Ultima III, Rigaku Corp., Japan) was carried out in the diffraction angle from 10º to 90º to identify the crystalline phase.

Results and Discussion

Macroporous Morphology

An appearance of as-dried sample is shown in Fig. 1a, and SEM images of as-dried samples with varied W_{PAAm} (setting the total volume of water at 2.75 mL) are depicted in Fig. 1b-f. In the case without PAAm, phase separation did not occur during the gelation, which indicates non-porous structure in the micrometer range (Fig. 1b). On the contrary, the addition of PAAm formed macroporous structure; morphologies changed from fragmented skeleton (Fig. 1c and 1d) to homogeneous co-continuous structure (Fig. 1e). Further increase in W_{PAAm} formed a continuous gel matrix embedded with isolated pores (Fig. 1f). Comparing samples prepared with and without PAAm, PAAm is preferentially distributed to the gel phase, evidenced by TG-DTA and FT-IR analysis (see ESI S1†).[19] Similarly to our previous work,[18] PAAm works not only as a phase separation inducer but also as a network former.

The effects of concentrations of water and glycerol on the morphology of as-dried samples are shown in Fig. 2a. The total volume of solvents, (V_{H2O} + V_{GLY} + W_{PAAm} x 0.5), was set at 4.75 mL, while the values of V_{H2O} or V_{GLY} were varied. Macroporous structures were remarkably changed; in samples prepared with the water concentration exceeding that of glycerol, large macropore was formed (Fig. 2a (i)), while a relative increase in glycerol concentration brought about smaller macropore size (Fig. 2a (ii)-(iii)). With the increase in the concentration of glycerol, pore size decreases as shown in Fig. 2b determined by mercury porosimetry; macropore size and porosity were 1.29 µm and 72% (i), 702 nm and 67% (ii), and 550 nm and 67% (iii), respectively. They are in good agreement with the values estimated from SEM images. Further increase in glycerol led to
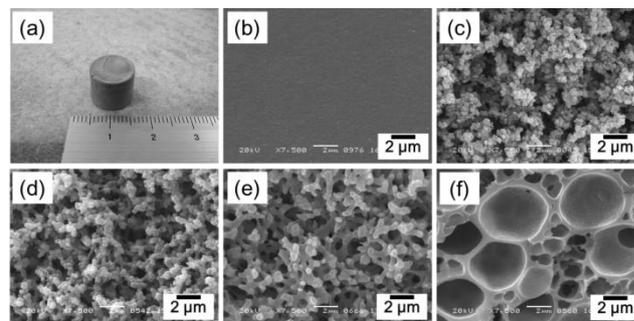

Fig. 1 (a) Appearance of as-dried sample, and SEM images of as-dried samples with varied W_{PAAm}; (b) 0.0 g, (c) 0.5 g, (d) 1.0 g, (e) 1.5 g, and (f) 2.0 g.
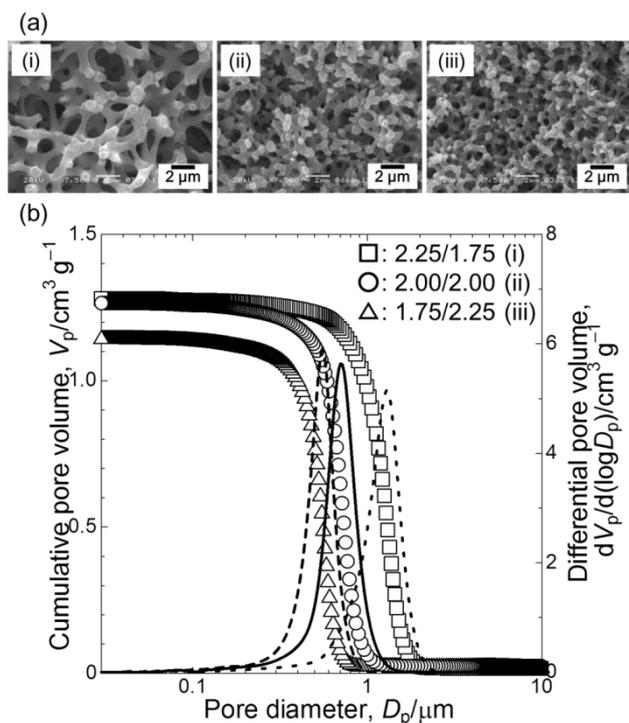
Fig. 2 (a) SEM images of as-dried samples with varied volume ratio of V_{H2O}/V_{GLY}; (i) 2.25/1.75, (ii) 2.00/2.00, and (iii) 1.75/2.25, respectively. (b) Macropore size distribution and cumulative pore volume of the samples (i)-(iii).

the formation of fine structure with smaller macropores (see ESI S2†). A solvent composition affects the co-continuous macrostructure owing to the solution viscosity and coordination effect derived from both glycerol and PAAm. Considering glycerol is partly distributed to the gel phase, similarly to the previous synthesis, the interaction between metal hydroxide species and organic functional groups plays an important role.[20] Since there is no big difference in the gelation time among the samples shown in Fig. 2a-c (about 2-3 min in all cases), the development of phase separation depends largely upon the kinetic factors that is influenced by the relative amounts of water and glycerol. The viscosity of glycerol-water solvent in the present synthetic condition (from 50 wt% to 80 wt% of glycerol in aqueous solution) differs by order of magnitude,[21] which caused the change of the development of phase separation to form different phase-separated structure as shown in Fig. 2a-c.

A change in the ratio Zn/Fe, R, influenced the morphology of as-dried gels, shown in Fig. 3a-f. When R is small, that is, the
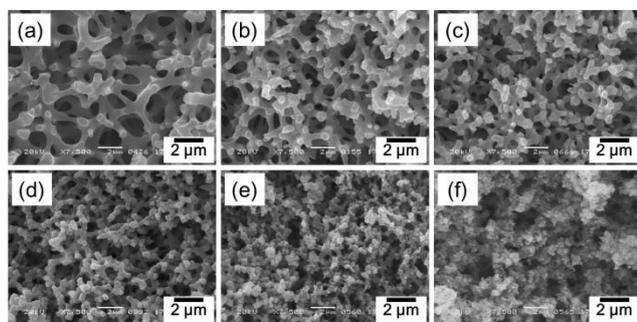

Fig. 3 SEM images of as-dried samples with varied the Zn/Fe ratio, R; (a) 0.20, (b) 0.33, (c) 0.50, (d) 1.00, (e) 1.50, and (f) 2.00, respectively.

amount of Fe(III) is large compared to that of Zn(II), a well-developed phase-separated structure, i.e. coarsened co-continuous structure was frozen (Fig. 3a). With an increase in the value of R, co-continuous structure became finer as depicted in Fig. 3b-d, and when R becomes excessively large, fragmented co-continuous structure was formed (Fig. 3e-f). Without adding any iron(III) hexahydrate, no gelation took place, and only aggregation of spherical particles without micrometer-ranged network was observed (see ESI S3†). The results suggest that the continuous skeleton in the micrometer range mainly consists of iron(III) hydroxide-based species. Cui *et al.* proposed that in the synthesis of $AlCo_2O_4$ nanoparticles by epoxide-mediated sol-gel reaction, aluminum hydroxide-based gel was firstly formed without any precipitation of cobalt hydroxide-based species, and then hydrated cobalt species reacted with aluminum hydroxide-based species at the skeleton surface; aluminum core with cobalt shell.[14] Also in the case of preparation of $ZnFe_2O_4$, $[Fe(H_2O)_6]^{3+}$ in the mixed solution may have similarly enhanced the reactivity of $[Zn(H_2O)_6]^{2+}$, resulting in simultaneous hydrolysis and condensation to form iron hydroxide at the core and zinc hydroxide at the shell.[14] The heterogeneity in hydroxide clusters grown in the solution containing multiple kinds of aquo-cations can be confirmed as follows. In the epoxide-mediated sol-gel method, aquo-cation behaves as an acid in solution to promote the hydrolysis and condensation, and its acidity can be evaluated by pK_a: acidity of M^{X+} decreases in the order of $X = 4 > 3 > 2$.[12] In the present research, there is a large difference in pK_a between $[Fe(H_2O)_6]^{3+}$ and $[Zn(H_2O)_6]^{2+}$ (2.2 and 9.5, respectively[52-53]), which led to the drastic morphological change with varied R, shown in Fig. 3. In the case of small R, co-continuous skeleton composed of mainly iron(III) hydroxide-based species was formed (Fig. 3a-b). On the other hand, when R is excessively large, the proportion of quickly precipitating $[Fe(H_2O)_6]^{3+}$ was too small to form continuous network of gels (Fig. 3d-f). Besides, the aggregation of spherical particles observed in the case only zinc chloride present (see ESI S3†) is also accounted for by kinetic factor of precipitation that depends on pK_a. Although hydrolysis and condensation of $[Zn(H_2O)_6]^{2+}$ occurs homogeneously, the degree of pH increase in this synthetic route is not so high enough to form zinc-based continuous gel network, resulting in the formation of homogeneous particles without micrometer-ranged network. After the heat-treatment under air, as-dried samples crystallized into $ZnFe_2O_4$ ($R = 0.5$), α-Fe_2O_3 with $ZnFe_2O_4$ ($0.20<R<0.50$), and ZnO with $ZnFe_2O_4$ ($0.50<R<2.00$), respectively (see ESI S4†).

Heat-Treatment and Meso/Micropores

Heat-treatment under air or Ar condition was carried out for samples prepared with $V_{H2O} = 2.00$ mL, $V_{GLY} = 2.00$ mL, and $W_{PAAm} = 1.5$ g. SEM pictures of samples calcined in air at 200 ºC and 300 ºC are shown in Fig. 4a, indicating co-continuous porous structures were not spoiled. However, detailed information about pore structure could not be examined since monolithic form was lost to give fragmented pieces through the heat-treatment possibly due to the decomposition of glycerol in skeletons.[18] Fig. 4b displays XRD patterns of samples as-dried and heat-treated in air at different temperatures. No specific peaks were observed in as-dried sample and that heat-treated at 200 ºC, because of the poor crystallinity in this synthetic condition. Diffraction peaks ascribed to zinc ferrite, $ZnFe_2O_4$, appeared during the heat-
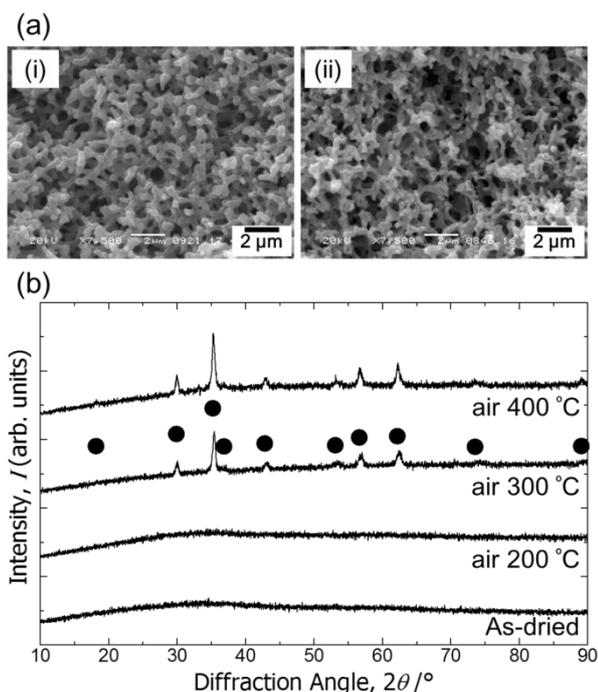
Fig. 4 (a) SEM images of samples calcined in air at 200 ºC (i) and 300 ºC (ii). (b) XRD patterns of as-dried and heat-treated samples at different temperature. Closed circle indicates ZnFe₂O₄ crystalline phase.

treatment in air above 300 ºC. After the heating under air, the elemental analysis using EDX was carried out, which indicated the Zn/Fe ratio calculated from the counts of characteristic X-ray generated was close to the stoichiometric value (Zn/Fe = 0.42) as depicted in ESI S5a† and ESI S6†. The decomposition of organic species in skeleton brought about the crystallization to $ZnFe_2O_4$ as well as collapse of monolithic form similarly to previous report.[18] On the other hand, Fig. 5a SEM images indicate both macroporous morphologies and monolithic form were perfectly preserved after the heat-treatment under Ar atmosphere at various temperatures. While shrinkage of macropore and monolithic form was observed, macropore of sample heated at 600 ºC was maintained as evidenced by the mercury intrusion result (see ESI S6†). After the calcination, with evolution of heating temperature, iron-based crystalline phases were mainly observed: Fe_3O_4 (or $ZnFe_2O_4$; the difference could not be clarified due to the same crystalline structure, spinel), $Fe_{1-\delta}O$, Fe_3N, Fe_4N, Fe_3C and metallic Fe (Fig. 5b). Generally, under an inert gas flow calcination, organic species become carbon, which behave as a reducing agent to induce "carbothermal reduction".[22] The carbon in skeleton triggers the formation of different partially/fully reduced crystalline phases. Dried gel skeleton obtained consists of core-shell type hydroxide-based species; iron hydroxide core and zinc hydroxide shell, similarly to $AlCo_2O_4$ system discussed above.[14] Similar heat-treatment of iron(III)-based gels in our previous research led to the formation of metallic iron from iron hydroxide at relative low temperature. It is highly possible that zinc-based species are easily reduced to metallic zinc under this strong reductive atmosphere.[18] Since it is well-known that metallic zinc exhibits remarkably low melting point about 419 ºC and high vapor pressure,[23] molten zinc thus generated at the surface is possibly swept by the gas flow (1 L min⁻¹) during the calcination, resulting in the absence of zinc-based crystalline phase. EDX analysis was carried out to investigate the amount of
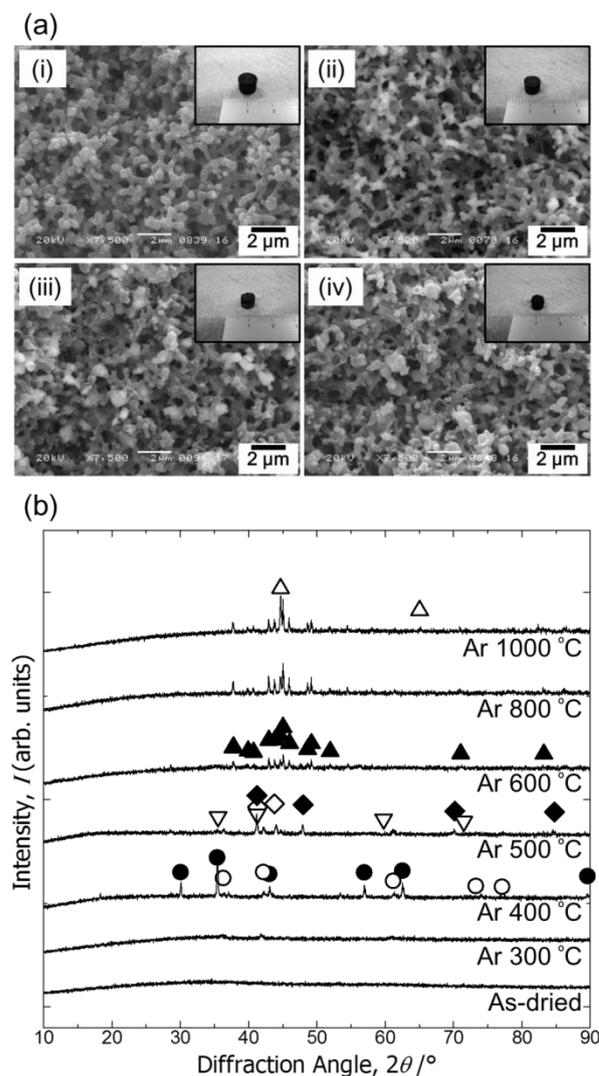

Fig. 5 (a) SEM images of samples calcined under Ar at 400 ºC (i), 500 ºC (ii), 800 ºC (iii), and 1000 ºC (iv). Insets show appearances of heat-treated samples. (b) XRD patterns of sample calcined under Ar at varied temperature. Symbols indicate as follows: closed circle is Fe_3O_4 (or $ZnFe_2O_4$), open circle is $Fe_{0.942}O$, inverted open triangle is $Fe_{0.945}O$, open rhombus is Fe_3N, closed rhombus is Fe_4N, closed triangle is Fe_3C, and open triangle is Fe, respectively.

zinc and iron at the surface for samples after the heat-treatment in air (a) and Ar (b) (see ESI S5†). Compared to the heat-treatment under air, the Zn/Fe ratio represents lower value in an inert condition (Zn/Fe = 0.08~0.22, summarized in ESI S6†), which indicates zinc-based species at the surface decrease through the heat-treatment under Ar flow.

In the samples heated under Ar, nanometer-sized pore was formed to contribute large surface areas characterized by nitrogen sorption measurement in Fig. 6. Both as-dried sample and that heated under Ar at 300 ºC possess no nanometer-sized pores, whereas further increase in temperature led to the formation of mesopore about 5-6 nm and micropore, resulting in large BET surface areas: 12 m²g⁻¹ for as-dried, 19 m²g⁻¹ at 300 ºC, 82 m²g⁻¹ at 400 ºC, 116 m²g⁻¹ at 500 ºC, 179 m²g⁻¹ at 800 ºC, and 163 m²g⁻¹ at 1000 ºC. BET surface areas and pore size distribution in inset
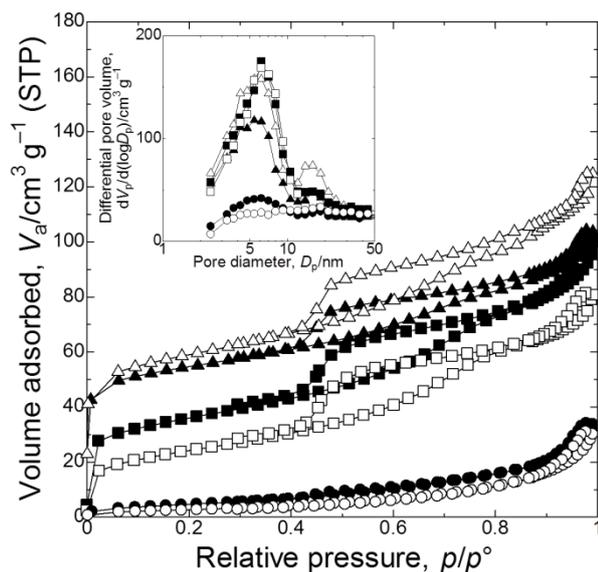
Fig. 6 N₂ sorption isotherms of as-dried sample and that of heated in Ar. Inset indicates pore size distribution. Symbols indicate as follows: open circle is as-dried, closed circle is Ar 300 ºC, open square is Ar 400 ºC, closed square is Ar 500 ºC, open triangle is Ar 800 ºC, and closed triangle is Ar 1000 ºC, respectively.

indicates the amount of nanometer-sized pores reaches a maximum at 800 ℃, and then calcination at higher temperature brought about the shrinkage of skeleton, which resulting in the decrease in the amount of nanometer-sized pores. In all cases, mesopore derives from interstices between primary particles in skeleton, and micropore does from the pyrolysis of carbon, which contribute large specific surface areas.

Conclusions

In summary, spinel type zinc ferrite, ZnFe₂O₄, with well-defined macropores has been successfully synthesized for the first time via an epoxide-mediated sol-gel process accompanied by phase separation. The macroporous morphologies could be controlled simply by the starting composition (macropore diameter ranges from 0.55 to 1.29 µm). The crystallization to zinc ferrite took place by heat-treatment in air above 300 ℃ with preserving macroporous co-continuous structure, while calcination under Ar atmosphere formed various crystalline phases/carbon composites (Fe₃O₄, Fe₁₋δO, Fe₃N, Fe₄N, Fe₃C, and Fe) without spoiling co-continuous structures as well as monolithic forms. Obtained samples heated under Ar atmosphere possess hierarchically pores, macropore, mesopore, and micropore to contribute large specific surface areas.

Notes

Department of Chemistry, Graduate School of Science, Kyoto University, Kitashirakawa, Sakyo-ku, Kyoto 606-8502, Japan. Fax: +81-75-753-2925; Tel: +81-75-753-2925; E-mail: kazuki@kuchem.kyoto-u.ac.jp
† Electronic Supplementary Information (ESI) available: [TG-DTA, FT-IR, SEM images, XRD patterns, EDX analysis, mercury intrusion]. See DOI: 10.1039/b000000x/

References

1 Z. Chen, E. Shi, W. Li, Y. Zheng, W. Zhong, *Mater. Lett.* 2002, **55**, 281; M. Llusar, A. Forés, J. A. Badenes, J. Calbo, M. A. Tena, G. J. Monrós, *J. Eur. Ceram. Soc.* 2001, **21**, 1121; J. H. Meng, G. Q. Yang, L. M. Yan, X. Y. Wang, *Dyes Pigm.* 2005, **66**, 109; J. I. Di Cosimo, V. K. Díez, M. Xu, E. Iglesia, C. R. Apesteguía, *J. Catal.* 1998, **178**, 499

2 H. G. Beljers, D. Polder, *Nature* 1950, **165**, 798; I. H. Gul, W. Ahmed, A. Maqsood, *J. Magn. Magn. Mater.* 2008, **320**, 270

3 Q. Yu, W. Holmes, K. Naishadham, *IEEE Trans. Electromagn. Compat.* 2002, **44**, 258; A. N. Yusoff, M. H. Abdullah, S. H. Ahmad, S. F. Jusoh, A. A. Mansor, S. A. A. Hamid, *J. Appl. Phys.* 2002, **92**, 876; Ö. Yavus, M. K. Ram, M. Aldissi, P. Poddar, H. Srikanth, *Synth. Met.* 2005, **151**, 211; M. C. Song, K. J. Lee, *Nucl. Eng. Des.* 2004, **229**, 101; K. Polychronopoulou, F. C. Galisteo, M. L. Granados, J. L. G. Fierro, T. Bakas, A. M. Efstathiou, *J. Catal.* 2005, **236**, 205; P. Lavela, J. L. Tirado, *J. Power Sources* 2007, **172**, 379; H. Lv, L. Ma, P. Zeng, D. Ke, T. Peng, *J. Mater. Chem.* 2010, **20**, 3665

4 M. R. Meshram, N. K. Agrawal, B. Sinha, P. S. Mistra, *J. Magn. Magn. Mater.* 2004, **271**, 207

5 R. T. Olsson, M. A. AziziSamir, G. Salazar-Alvarez, L. Belova, V. Ström, L. A. Berglund, O. Ikkala, J. Nogués, U. W. Gedde, *Nat. Nanotechnol.* 2010, **5**, 584; Y. Zhai, J. Zhai, M. Zhou, S. Dong, *J. Mater. Chem.* 2009, **19**, 7030; J. Haetge, C. Suchomski, T. Brezesinski, *Inorg. Chem.* 2010, **49**, 11619; C. Reitz, C. Suchomski, J. Haetge, T. Leichtweiss, Z. Jagličić, I. Djerdj, T. Brezesinski, *Chem. Comm.* 2012, **48**, 4471

6 F. S. Li, L. Wang, J. B. Wang, Q. G. Zhou, X. Z. Zhou, H. P. Kunkel, G. Williams, *J. Magn. Magn. Mater.* 2004, **268**, 332

7 H. Minakuchi, K. Nakanishi, N. Soga, N. Ishizuka, N. Tanaka, *Anal. Chem.* 1996, **68**, 3498; N. Nakamura, R. Takahashi, S. Sato, T. Sodesawa, S. Yoshida, *Phys. Chem. Chem. Phys.* 2000, **2**, 498

8 Y. I. Kim, D. Kim, C. S. Lee, *Physica B* 2003, **337**, 42; S. D. Shenoy, P. A. Joy, M. R. Anantharaman, *J. Magn. Magn. Mater.* 2004, **269**, 217; X. J. Xu, L. H. Zhou, Q. G. Zhai, C. Z. Lu, *J. Am. Ceram. Soc.* 2007, **90**, 1959; P. Lee, H. Suematsu, W. Jiang, K. Yatsui, *J. Ceram. Soc. Jpn.* 2005, **113**, 663; K. V. P. M. Shafi, A. Gedanken, *Chem. Mater.* 1998, **10**, 3445; A. E. Baranchikov, V. K. Ivanov, N. N. Oleinikov, Y. D. Tret'yakov, *Inorg. Mater.* 2004, **40**, 1091; C. T. Seip, E. E. Carpenter, C. J. O'connor, *IEEE Trans. Magn.* 1998, **34**, 1111; N. Bao, L. Shen, Y. Wang, P. Padhan, A. Guputa, *J. Am. Chem. Soc.* 2007, **129**, 12374; D. H. Chen, X. R. He, *Mater. Res. Bull.* 2001, **36**, 1369; R. J. Zhang, J. J. Huang, H. T. Zhao, Z. Q. Sun, Y. Wang, *Energy Fuels* 2007, **21**, 2682; P. Brown, L. J. Hope-Weeks, *J. Sol-Gel Sci. Technol.* 2009, **51**, 238; S. Xuan, F. Wang, Y. X. J. Wang, J. C. Yu, K. Cham-Fai Leung, *J. Mater. Chem.* 2010, **20**, 5086

9 M. Veith, M. Haas, V. Huch, *Chem. Mater.* 2005, **17**, 95

10 A. E. Gash, T. M. Tillotson, J. H. Satcher Jr., J. F. Poco, L. W. Hrubesh, R. L. Simpson, *Chem. Mater.* 2001, **13**, 999

11 A. E. Gash, T. M. Tillotson, J. H. Satcher Jr., L. W. Hrubesh, R. L. Simpson, *J. Non-Cryst. Solids* 2001, **285**, 22

12 A. E. Gash, J. H. Satcher Jr., R. L. Simpson, *J. Non-Cryst. Solids* 2004, **350**, 145

13 C. N. Chervin, B. J. Clapsaddle, H. W. Chiu, A. E. Gash, J. H. Satcher Jr., S. M. Kauzlarich, *Chem. Mater.* 2006, **18**, 4865; H. Cui, M. Zayat, D. Levy, *J. Non-Cryst. Solids*, 2005, **351**, 2102

14 H. Cui, M. Zayat, D. Levy, *J. Sol-Gel Sci. Technol.* 2005, **35**, 175

15 Y. Tokudome, K. Fujita, K. Nakanishi, K. Miura, K. Hirao, *Chem. Mater.* 2007, **19**, 3393

16 K. Nakanishi, *J. Porous Mater.* 1997, **4**, 67

17 Y. Tokudome, K. Fujita, K. Nakanishi, K. Kanamori, K. Miura, K. Hirao, T. Hanada, *J. Ceram. Soc. Jpn.* 2007, **115**, 925; Y. Tokudome, A. Miyasaka, K. Nakanishi, K. Kanamori, T. Hanada, *J. Sol-Gel Sci. Technol.* 2011, **57**, 269; G. Hasegawa, Y. Ishihara, K. Kanamori, K. Miyazaki, Y. Yamada, K. Nakanishi, T. Abe, *Chem. Mater.* 2011, **23**, 5208

18 Y. Kido, K. Nakanishi, A. Miyasaka, K. Kanamori, *Chem. Mater.* 2012, **24**, 2071

19 M. Tutas, M. Saglam, M. Yuksel, C. Guler, *Thermochim. Acta* 1987, **111**, 121; R. M. Silverstein, F. X. Webster, D. J. Kiemle, *Infrared*

Spectrometry: Spectrometric Identification of Organic Compounds, 7th ed.; John Wiley & Sons, Inc.: New York, 2005; pp 99-101.

20 J. Rubio, E. Matijevic, *J. Colloid. Interface Sci.* 1979, **68**, 408; J. Wen, V. J. Vasudevan, G. L. Wilkes, *J. Sol-Gel Sci. Technol.* 1995, **5**, 115

21 J. B. Segur, H. E. Oberstar, *Ind. Eng. Chem.* 1951, **43**, 2117

22 J. Li, C. L. Fisher, J. L. Chen, D. Bashford, L. Noodleman, Inorg. Chem. 1996, **35**, 4694; R. A. Mathews, C. S. Rossiter, J. R. Morrow, J. P. Richard, Dalton Trans. 2007, **34**, 3804

23 J. Barker, M. Y. Saidi, J. L. Swoyer, *Solid-State Lett.* 2003, **6**, A53

24 D. R. Stull, Ind. Eng. Chem. 1947, **39**, 517

Sol-Gel Synthesis of Zinc Ferrite-Based Xerogel Monoliths with Well-Defined Macropores

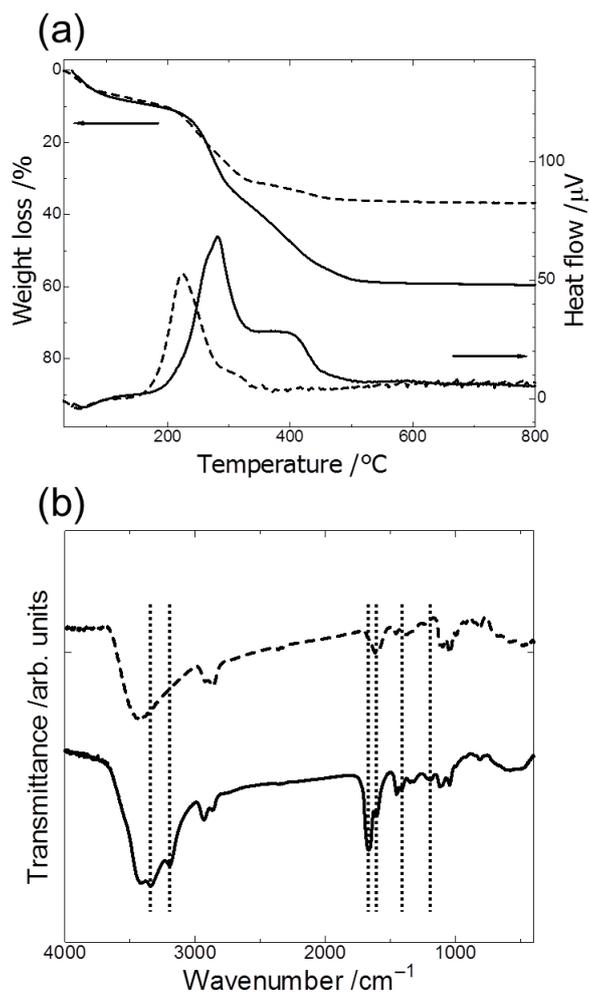**Yasuki Kido, Kazuki Nakanishi,* and Kazuyoshi Kanamori**

Fig. S1   (a) TG-DTA curves for gel phase of as-dried samples prepared without PAAm (dashed lines) and with PAAm (solid lines).   Weight loss and exothermic peaks from 200 ℃ to 300 ℃ observed in both samples are ascribed to crystallization to $ZnFe_2O_4$ and decomposition of glycerol, and those from 300 ℃ to 400 ℃ observed in sample prepared with PAAm is the combustion of PAAm.   (b) FT-IR spectra of as-dried samples prepared without PAAm (dashed line) and with PAAm (solid line).   Dotted lines indicate as following bondings: C-N for 1,196 cm^{-1}, CH$_2$ for 1,420 cm^{-1}, N-H for 1,604 cm^{-1}, 3,196 cm^{-1}, and 3,342 cm^{-1}, and C=O for 1,664 cm^{-1}, respectively. Appearance of new bands and intensity growth derived from PAAm are observed.
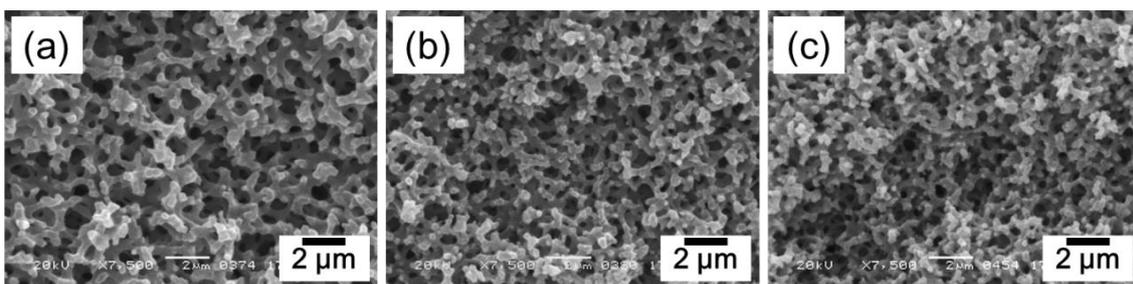
Fig. S2　SEM images of as-dried samples with varied volume ratio of V_{H2O}/V_{GLY}; (a) 1.50/2.50, (b) 1.25/2.75, and (c) 1.00/3.00, respectively.　With increased the amount of glycerol, macrostructures become finer.
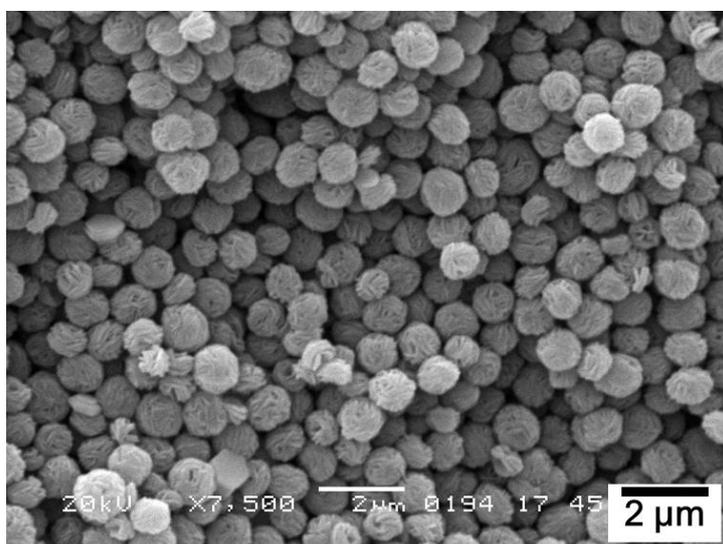

Fig. S3　SEM image of as-dried sample synthesized from only zinc chloride as a metal precursor without adding any iron(III) chloride hexahydrate.　No micrometer-ranged skeleton was observed, and the aggregation of spherical particles less than 1 μm was formed.
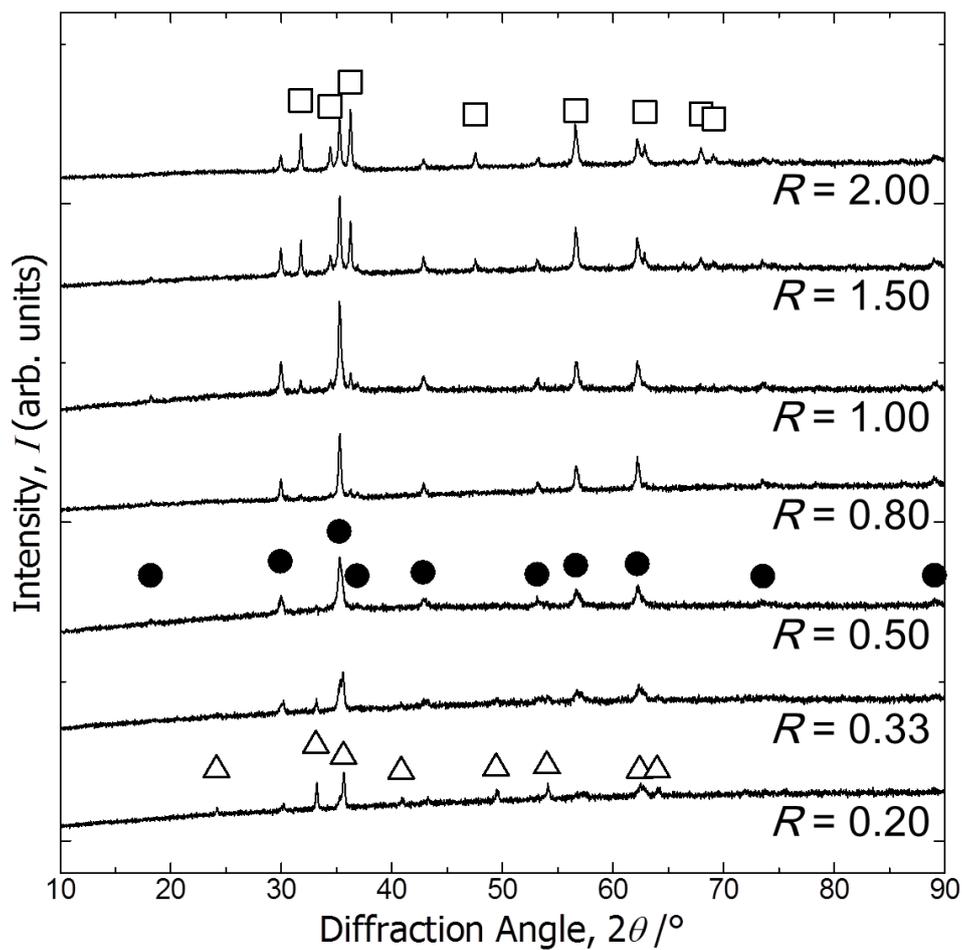
Fig. S4   XRD patterns of samples heat-treated in air at 300 ℃ for 4 h with varied the ratio of Zn to Fe, R, from 0.20 to 2.00.   Symbols indicate as follows: open triangle is α-Fe_2O_3, closed circle is $ZnFe_2O_4$, and open square is ZnO, respectively.   With increasing R, crystalline phase changes from α-Fe_2O_3 through $ZnFe_2O_4$ to ZnO.
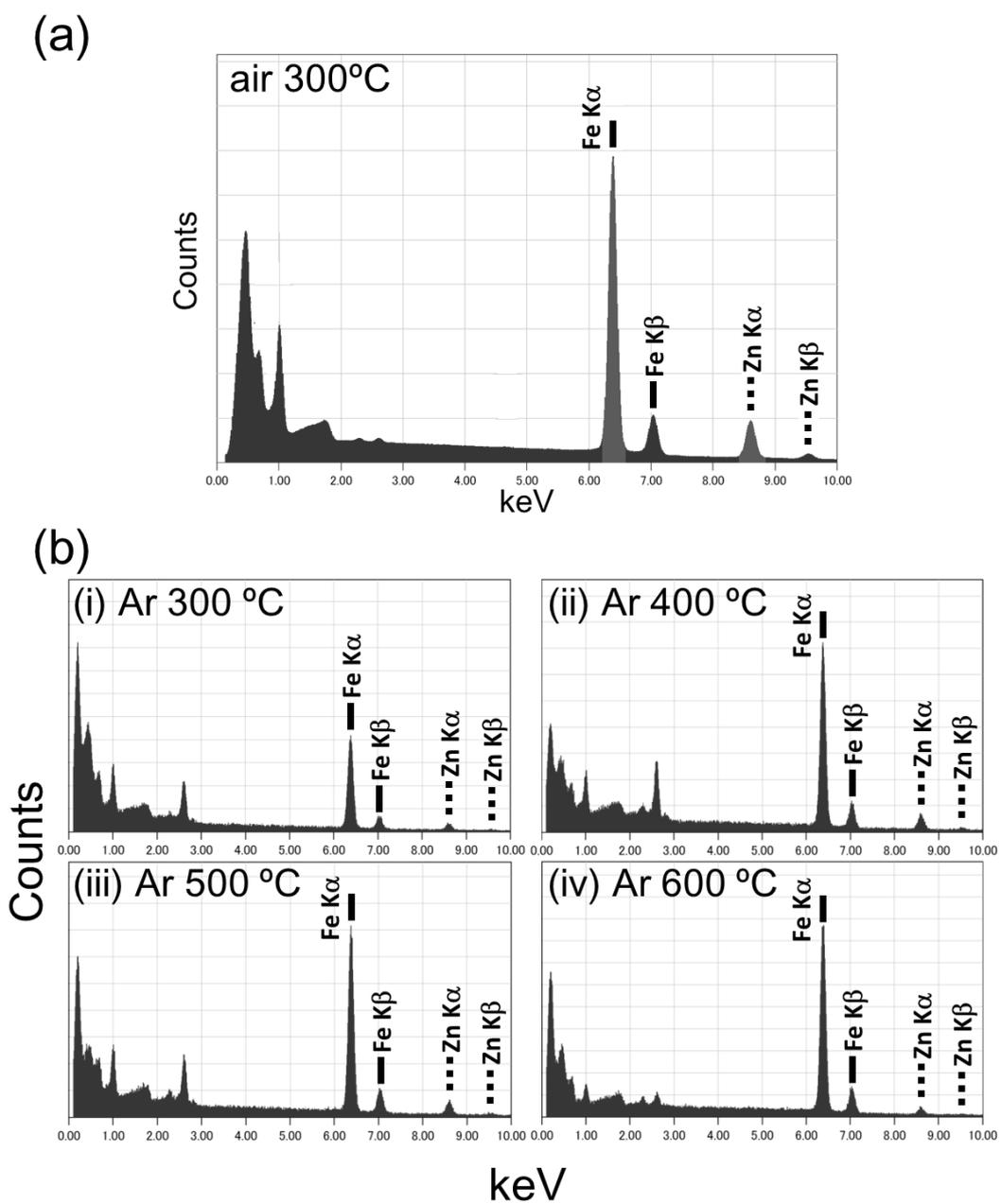
Fig. S5　EDX analysis of samples calcined under (a) air, and (b) Ar flow at different temperature.

Table S6.   Caicination condition and the Zn/Fe ratio calculated from EDX analysis depicted in Fig. S5.   Under air heat-treatment, Zn/Fe is close to 0.50, which is starting composition, on the other hand, Zn/Fe decreases to 0.08~0.22 under Ar heat-treatment, which results indicates there are few zinc-based species at the surface.

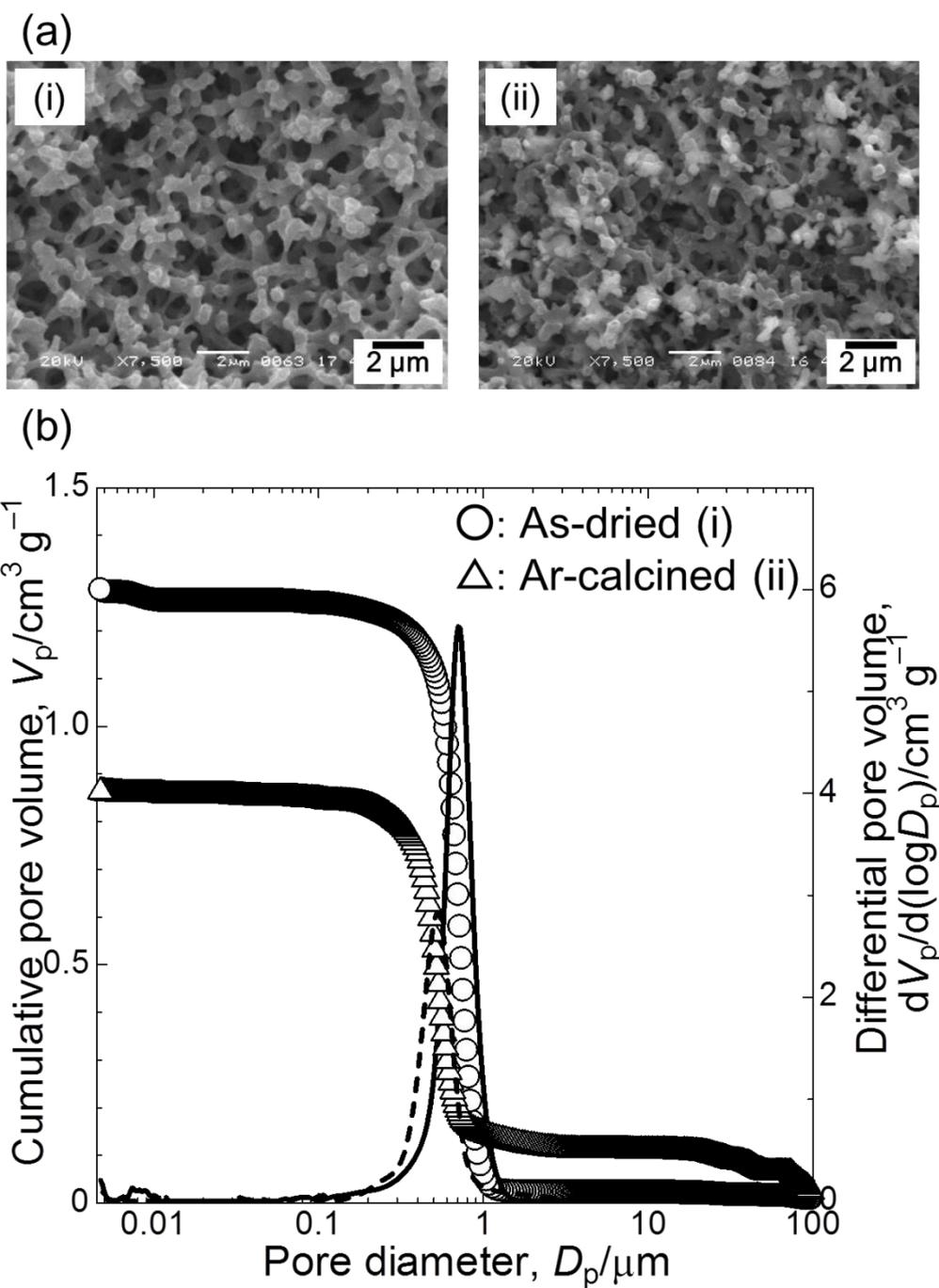| Calcination Condition	Zn/Fe
air 300 ℃, 4 h	0.42
Ar 300 ℃, 4 h (with continuous Ar flowing)	0.20
Ar 400 ℃, 4 h (with continuous Ar flowing)	0.22
Ar 500 ℃, 4 h (with continuous Ar flowing)	0.19
Ar 600 ℃, 4 h (with continuous Ar flowing)	0.08

Fig. S7　(a) SEM images of (i) as-dried sample and (ii) that of heated under Ar at 600 ℃.　(b) Mercury intrusion results indicate macropore size distribution and cumulative pore volume; as-dried sample (open circle) and calcined sample (open triangle).　Heat-treated sample also possessed well-defined macropore about 533 nm.　Compared to as-dried sample, shrinkage of macropore as well as reduction of cumulative pore volume was observed.